The Astrophysical Journal, 743:154 (14pp), 2011 December 20 doi:10.1088/0004-637X/743/2/154

CONSTRAINING GAMMA-RAY BURST EMISSION PHYSICS WITH EXTENSIVE EARLY-TIME, MULTIBAND FOLLOW-UP

A. Cucchiara[1,2], S. B. Cenko[1], J. S. Bloom[1], A. Melandri[3,4], A. Morgan[1], S. Kobayashi[4], R. J. Smith[4], D. A. Perley[1], W. Li[1], J. L. Hora[5], R. L. da Silva[2,9], J. X. Prochaska[2], P. A. Milne[6], N. R. Butler[1], B. Cobb[7], G. Worseck[2], C. G. Mundell[4], I. A. Steele[4], A. V. Filippenko[1], M. Fumagalli[2], C. R. Klein[1], A. Stephens[8], A. Bluck[8], and R. Mason[8]

[1] Department of Astronomy, University of California, Berkeley, CA 94720-3411, USA; acucchia@ucolick.org

[2] Department of Astronomy and Astrophysics, UCO/Lick Observatory, University of California, 1156 High Street, Santa Cruz, CA 95064, USA

[3] INAF, Osservatorio Astronomicodi Brera, via E. Bianchi 46, I-23807 Merate (LC), Italy

[4] Astrophysics Research Institute, Liverpool John Moores University, Twelve Quays House, Egerton Wharf, Birkenhead, CH41 1LD, UK

[5] Harvard-Smithsonian Center for Astrophysics, 60 Garden St., Cambridge, MA 02138, USA

[6] Steward Observatory, University of Arizona, 933 N. Cherry Ave., Tucson, AZ 85719, USA

[7] Department of Physics, The George Washington University, Corcoran 105, 725 21st St, NW, Washington, DC 20052, USA

[8] Gemini Observatory, 670 North A'ohoku Place, Hilo, HI 96720, USA

Received 2011 July 15; accepted 2011 September 1; published 2011 December 2

ABSTRACT

Understanding the origin and diversity of emission processes responsible for gamma-ray bursts (GRBs) remains a pressing challenge. While prompt and contemporaneous panchromatic observations have the potential to test predictions of the internal–external shock model, extensive multiband imaging has been conducted for only a few GRBs. We present rich, early-time, multiband data sets for two *Swift* events, GRB 110205A and GRB 110213A. The former shows optical emission since the early stages of the prompt phase, followed by the steep rising in flux up to ∼1000 s after the burst ($t^{-\alpha}$ with $\alpha = -6.13 \pm 0.75$). We discuss this feature in the context of the reverse-shock scenario and interpret the following single power-law decay as being forward-shock dominated. Polarization measurements, obtained with the RINGO2 instrument mounted on the Liverpool Telescope, also provide hints on the nature of the emitting ejecta. The latter event, instead, displays a very peculiar optical to near-infrared light curve, with two achromatic peaks. In this case, while the first peak is probably due to the onset of the afterglow, we interpret the second peak to be produced by newly injected material, signifying a late-time activity of the central engine.

Key words: gamma-ray burst: individual (GRB 110205A, GRB 110213A) – techniques: photometric – techniques: polarimetric – techniques: spectroscopic

Online-only material: color figures, machine-readable tables

1. INTRODUCTION

Despite the unassailable utility of gamma-ray bursts (GRBs) as probes of the universe (e.g., Tanvir et al. 2009; Totani et al. 2006; Salvaterra et al. 2009; Cucchiara et al. 2011), some basic questions about the nature of the emission mechanisms persist. The *internal–external* shock paradigm, whereby the prompt gamma rays arise from self-shocking of an unsteady relativistic wind (Kobayashi & Zhang 2003; Sari & Piran 1997) and the afterglow arises from shock interaction with the ambient medium (Zhang et al. 2003), has found support (e.g., Guidorzi et al. 2011; Shao & Dai 2005) and challenges (Zhang 2011) from observations. The role of the *reverse* shock—that crossing back through the ejecta—in the dynamics and observables remains largely unconstrained owing to the lack of good early-time multicolor observations when the reverse-shock contribution should be most prominent. In the pre-*Swift* era only a handful of GRBs were detected with sufficient temporal resolution, but an unambiguous case of reverse-shock contribution was not established (Kobayashi 2000; Zhang et al. 2003; Gruber et al. 2011; Perley et al. 2008; Gomboc et al. 2008; Mundell et al. 2007a). The *Swift* satellite (Gehrels et al. 2004) has permitted unprecedented observations of GRBs at early times (Vestrand et al. 2006; Klotz et al. 2008), allowing rapid investigation of emission from hard X-ray to optical frequency regimes. Similarly, fast-response, robotic ground-based telescopes have been optimized in order to quickly follow up *Swift* events. Thanks to a trigger rate of 100 events/year, a large variety of GRBs have been observed, showing several different characteristics. For example, afterglows have shown more transitional phases in their light curves than pre-*Swift* samples (Evans et al. 2009). In some cases, they show optical and X-ray flares, indicating a refreshing activity from the central engine (Falcone et al. 2007). All of this new information has made the quest for a "standard model" very challenging, and, after six years of investigation, is still not fully understood.

In this paper, we detail high-energy *Swift* observations of GRB 110205A and GRB 110213A, and associated ground-based observations from several facilities typically starting around the end of the prompt emission. Multiband observations, spanning several orders of magnitude in frequency and time, in combination with afterglow spectroscopy and host galaxy imaging, represent two extensive data sets in order to further investigate the *reverse*-shock emission (see also Gao 2011). In Sections 2 and 3, we present our data sets and the data analysis procedure; in Section 4 we show our light curves and spectral energy distribution (SED) modeling analysis, and the uncertainties involved in the theoretical modeling. Finally, Section 5 will summarize our findings and discuss some of the future prospects of GRB investigation. Throughout the paper all errors are quoted as a 90% confidence interval, unless

[9] NSF Graduate Research Fellow.

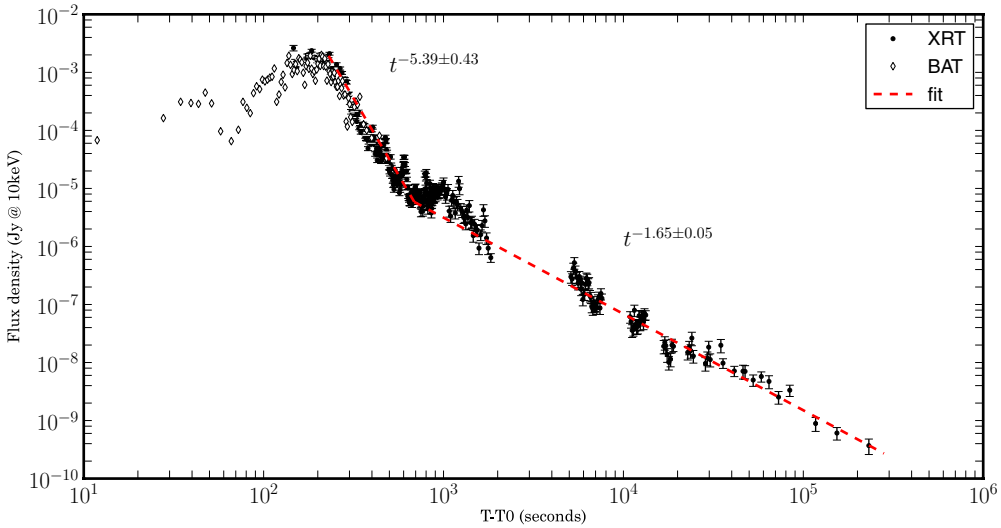

Figure 1. GRB110205A BAT (open diamonds) and XRT (filled circles) light curve. The BAT emission is rescaled to the XRT energy bands using a spectral index $\Gamma_{\rm ave} = 1.59$ (see Section 4.1.1). Dashed lines indicate the different power-law segments obtained by fitting the XRT data with single power laws.
(A color version of this figure is available in the online journal.)

otherwise noted. We use a standard cosmological model with $H_0 = 71$ km s^{-1} Mpc^{-1}, $\Omega_M = 0.27$, and $\Omega_\Lambda = 0.73$.

2. GRB 110205A DATA SET

2.1. Space-based Data

GRB 110205A was discovered by the *Swift* satellite on 2011 February 5 at $T_0 = 02{:}02{:}41$ (UT dates are used throughout this paper). The Burst Alert Telescope (BAT) instrument (Barthelmy et al. 2005) showed a complex structured emission in the 15–350 keV energy range (Beardmore et al. 2011a). The GRB light curve shows several overlapping peaks rising around $T_0 - 120$ s, with the tallest peak at $T_0 + 210$ s, and minor activity until $T_0 + 1500$ s. The duration of the main pulse, measured in the 15–350 keV energy range, was $T_{90} = 257 \pm 25$ s (Markwardt et al. 2011).

At the same time, the *Suzaku*-Wide-band All-sky Monitor observed the emission from this object in the 20–3000 keV energy range. Combined with the BAT data we constructed a joint spectrum in the energy range from 15 to 3000 keV, which is well fit by a power law with exponential cutoff model ($dN/dE \sim E^{\Gamma_\gamma} \times e^{-(2+\Gamma_\gamma)E/E_{\rm peak}}$). The best-fit spectral parameters are $\Gamma_\gamma = -1.59^{+0.07}_{-0.06}$ and $E_{\rm peak} = 230^{+135}_{-65}$ keV. The energy fluence in the 15–3000 keV band calculated for this model is $2.7^{+0.7}_{-0.4} \times 10^{-5}$ erg cm^{-2} (Sakamoto et al. 2011). Assuming this value and a redshift of $z = 2.22$ for GRB 110205A (see Section 2.4) the isotropic-equivalent energy released is $E_{\rm iso} = 4.34^{+0.4}_{-0.7} \times 10^{53}$ erg in the 1 keV to 10 MeV range (Pal'Shin 2011).

The X-ray Telescope (XRT; Burrows et al. 2005) started observing the field 155.4 s after the trigger and showed an uncataloged fading source at R.A. $= 10^{\rm h}58^{\rm m}31\farcs13$, decl. $= +67^\circ31'30\farcs8$ (J2000), with an uncertainty of $1\farcs5$ (90% confidence; Beardmore et al. 2011b). The XRT and BAT data were obtained from publicly available repositories (Evans et al. 2007, 2009; Butler et al. 2007; Butler & Kocevski 2007). At early times ($T \lesssim 10^3$ s; note that henceforth, T is often used as a shorthand substitute for $T - T_0$), the light curve displays complex behavior, due probably to the temporal overlap of different pulses similar to the pulses identified in the BAT data, as well as flaring activity. After the prompt phase, the X-ray afterglow declines until ~600 s with a steep power law ($\alpha_X = 5.39 \pm 0.43$). Finally, the late-time behavior ($T \gtrsim 10^3$ s) can be fitted by a single power law with decay index $\alpha_X = 1.65 \pm 0.05$. A double power law with decay indices $\alpha_{X,1} = 1.67 \pm 0.05$ and $\alpha_{X,2} = 2.01 \pm 0.34$ and a possible break time around ≈ 80 ks after the GRB explosion provides a slightly better fit, but not statistically significant. Some flares are clearly visible throughout the X-ray light curve, likely indicating a continuation of the progenitor activity (see Figure 1), as previously seen in other GRBs (Falcone et al. 2007).

Using the early-time data ("window-timing" mode), the XRT averaged spectrum can be fitted by an absorbed power-law model with photon index $\Gamma_X = 1.42 \pm 0.02$, while the late-time spectrum in the XRT energy bands can be fitted with an absorbed power law with a photon spectral index of $\Gamma_X = 1.99^{+0.08}_{-0.07}$. In this case, the best-fitted absorption column density, at $z = 2.22$, is $N_{\rm H} = 3.5^{+1.6}_{-1.5} \times 10^{21}$ cm^{-2}, in addition to the Galactic value of 1.6×10^{20} cm^{-2} (Kalberla et al. 2005).

Other space-based facilities provided additional high-energy coverage. The *Konus*-Wind experiment detected GRB 110205A in the 20–1200 keV energy range with a 4.5σ detection of a possible precursor at $T_0 - 1360$ s. In addition, a soft tail up to $T_0 + 1200$ s has been detected, consistent with a similar detection by the *Swift*-BAT instrument. The total fluence is $S = 3.66 \pm 0.35 \times 10^{-5}$ erg cm^{-2} in the 20–1200 keV range (Golenetskii et al. 2011a; Pal'Shin 2011).

Finally, 164 s after the BAT detection, the UVOT instrument (Roming et al. 2005) on board *Swift* began observing GRB 110205A, identifying the source in the *white*-band filter at R.A. $= 10^{\rm h}58^{\rm m}31\farcs12$ and decl. $= +67^\circ31'31\farcs2$ (J2000) with a $0\farcs63$ accuracy in both directions (Figure 2; Beardmore et al. 2011b). UVOT early-time observations have been acquired in "image-event" mode, allowing a very detailed time-resolved analysis of the count rate variation in the UVOT detector. Using the HEASOFT tools UVOTEVTLC and UVOTMAGHIST we estimated the total flux inside a 5″ region centered at the object position, while using an annular background region as suggested by Poole et al. (2008) and Breeveld et al. (2011). Data in the *white* filter were binned with a bin size of 8 s in order to reach a minimum signal-to-noise ratio (S/N) of 3 bin^{-1}, in particular during the prompt emission.

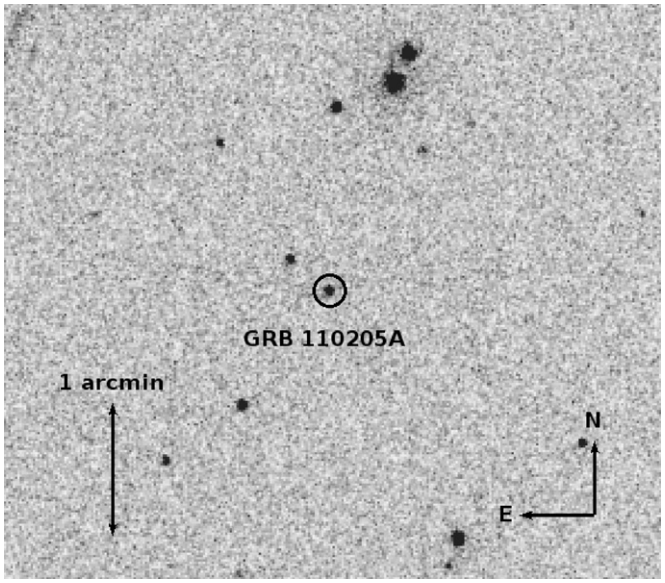

Figure 2. UVOT v band image of GRB 110205A obtained ∼1400 s after the trigger.

The afterglow was also detected in the u, b, v, and $w1$ filters up to $T = 8 \times 10^4$ s. The lack of detection in the other two, bluer, filters available on UVOT is consistent with the observed redshift.

2.2. Ground-based Follow-up

Soon after the *Swift* trigger, several robotic facilities pointed at the GRB location providing a series of photometric observations from optical to near-infrared (NIR) and radio bands. Our group first identified an infrared counterpart using the Peters Automated Infrared Imaging Telescope (PAIRITEL; Bloom et al. 2006) which consists of the 1.3 m Peters Telescope at Mt. Hopkins, AZ, formerly used for the Two Micron All Sky Survey (2MASS; Skrutskie et al. 2006), refurbished with the southern 2MASS camera. Observations began at 05:14:03, ∼3.2 hr after the trigger, and continued until the source reached its hour-angle limit. Further observations were obtained on the following day (Morgan et al. 2011; Morgan & Bloom 2011). The raw data files were processed using a standard IR reduction technique via PAIRITEL Pipeline III and resampled using SWarp[10] (Bertin et al. 2002) to create $1\farcs0$ pixel^{-1} images for final photometry.

The standard observing mode is to take three 7.8 s exposures in immediate succession at each dither position. These are then median-combined into 23.4 s "triplestacks," which were subsequently binned iteratively until a large enough S/N was achieved at the source position for accurate photometry. Aperture photometry was performed using custom Python software, utilizing Source Extractor (SExtractor; Bertin & Arnouts 1996) as a back end. Eight calibration stars present in all images were chosen based on brightness, proximity of nearby contaminating sources, and location relative to bad pixels. The optimal aperture of $4''$ diameter was determined by minimizing the absolute error relative to 2MASS magnitudes of our calibration stars.

Calibration was performed by redetermining the zero point for each image individually by comparison to 2MASS magnitudes using these eight stars. The resulting statistical uncertainty in the zero point is negligible relative to other sources of error. Additional, systematic sources of error are addressed in detail by Perley et al. (2010); we use a similar procedure here to determine the total uncertainty of each point.

We also observed the field of GRB 110205A with the automated Palomar 60 inch telescope (P60; Cenko et al. 2006) approximately 96 minutes after the *Swift*-BAT trigger time. After executing a series of pre-programmed g', r', i', and z' observations, we manually inserted deeper observations until the afterglow faded below our sensitivity threshold.

Basic processing (bias subtraction, flat fielding, etc.) was performed by our custom IRAF[11] pipeline. Later images were stacked to increase sensitivity with the SWarp software. Instrumental magnitudes were extracted using point-spread function fitting routines from the IRAF `DAOPHOT` package and were photometrically calibrated with respect to bright, nearby reference stars from the Sloan Digital Sky Survey (Abazajian et al. 2009).

Multiband observations of the optical afterglow of GRB 110205A were also acquired with the robotic 2 m Liverpool Telescope (LT) starting about 920 s after the trigger time. After taking a sequence of short exposures with the r' filter (6×10 s), the LT continued to monitor the field cycling through g', r', and i' filters, using increasing exposure times, until finishing about 155 minutes after the burst event. Two deeper, 300 s long, observations in the r' filter were acquired manually at the end of the night, when the optical transient (OT) was still clearly detected (see Figure 3). These observations were all photometrically calibrated using the same standard stars adopted for the Palomar data.

After ∼4.5 days, when the afterglow faded beyond the detectability of these facilities, we activated our Target of Opportunity (ToO) program at the Gemini-North telescope (PI: B. Cobb), in order to monitor the late-time behavior of the OT and/or estimate the possible host galaxy contribution. We performed a series of 10×3 minutes exposure in r' and i' bands using the Gemini Multi-Object Spectrograph (GMOS) camera (Hook et al. 2004). We analyzed and co-added these data sets using the dedicated `GEMINI` tool included in the IRAF environment. Calibration was performed using calibration stars present in the P60 data and magnitude were estimated using SExtractor.

The afterglow was detected and its brightness in the two bands is consistent with the extrapolation from early-time data, following a single power-law behavior.

In order to establish a possible host galaxy contribution, we repeated our r'-band observation on 2011 March 11. We collected a total exposure time of 40 minutes. No object is detected at a 3σ upper limit of $r' > 27.21$ mag, corresponding to a flux density limit of 4.88×10^{-2} μJy, implying no significant host contamination in our earlier observations. A summary of all our observations can be found in Table 1 and shown in Figure 3 with all our optical and infrared data.

The overall light curve in the optical and near-infrared bands after the first 300 s can be fitted by a model with two double power-law components known as "Beuermann functions" (Beuermann et al. 1999):

$$F_i(t) = \sum_{n=1,2} F_{i,n} \left[\left(\frac{t}{t_{b_n}} \right)^{\alpha_n} + \left(\frac{t}{t_{b_n}} \right)^{\beta_n} \right]^{-1}.$$

The normalization factors ($F_{i,n}$) are different for each of the i data sets and are free parameters in our fitting procedure, as well

[10] See http://www.astromatic.net/software/swarp.

[11] IRAF is distributed by the National Optical Astronomy Observatory, which is operated by the Association for Research in Astronomy, Inc., under cooperative agreement with the National Science Foundation.

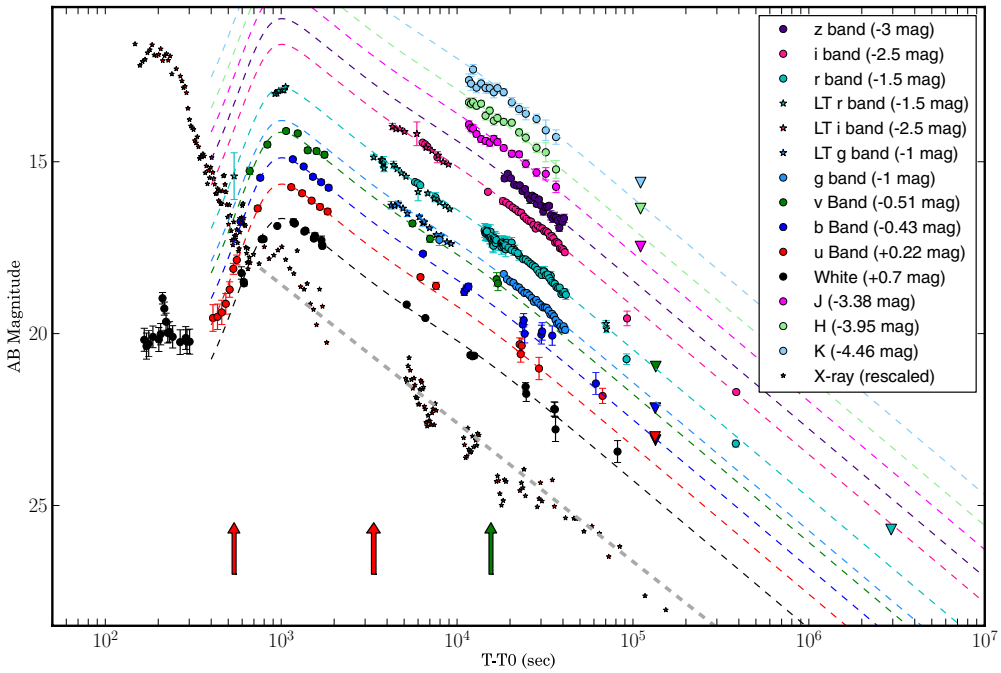

Figure 3. GRB110205A light curve. We present all the available public data in conjunction with the data sets present in this work. The dashed lines represent a resulting multiband fit (see Section 2 for more details). The XRT light curve is arbitrarily rescaled for comparison and fitted with a simple power-law function. The achromatic steep rise in the optical bands is interpreted as the signature of the reverse shock. After the peak at $T \approx 985$ s the forward shock is the main source of radiation, confirmed by the net polarization measurement obtained at the time of the RINGO2 and the CAFOS instrument observations, indicated with red and green arrows, respectively.

Table 1
Photometric Observations for GRB 110205A

$T - T_0$ (s)	Filter	Magnitude[a]	1σ Error
	Swift-UVOT		
166	*white*	18.68	0.34
171	*white*	18.86	0.38
176	*white*	18.79	0.38
186	*white*	18.59	0.31
201	*white*	18.67	0.35
206	*white*	18.52	0.31
211	*white*	17.47	0.17
216	*white*	17.77	0.19
221	*white*	18.15	0.25
226	*white*	18.48	0.29

Notes. [a] UVOT magnitudes are in the natural UVOT photometric system (Vega). See Breeveld et al. (2011) for the most updated zero point and conversion factors.

(This table is available in its entirety in a machine-readable form in the online journal. A portion is shown here for guidance regarding its form and content.)

as the power-law indices (α_n and β_n) and the break times (t_{b_n}), which are considered to be the same for all the bands. In this formalism, the peaks of the individual function can be estimated as

$$t_{\mathrm{peak},n} = t_{b_n} \times (-\alpha_n/\beta_n)^{1/(\beta_n-\alpha_n)}.$$

Both components are needed in order to account for the steep rise at early time and the exponential decay after the first peak at $t_{\mathrm{peak}} = 985 \pm 48$ s. We fit our data sets simultaneously and the results are listed in Table 2 as well as presented in Figure 3, before correcting for Galactic extinction, $E(B-V) = 0.02$.

In addition, radio observations were performed with several facilities providing upper limits in the millimeter and submillimeter regimes (Zauderer et al. 2011a; Petitpas et al. 2011; van der Horst et al. 2011). The Expanded Very Large Array facility detected the radio afterglow 1.2 days after the burst, providing a flux density of 182 ± 12 μJy at a frequency of 22 GHz (Zauderer et al. 2011b).

2.3. Optical Polarization

Polarization observations were obtained with the RINGO2 polarimeter on the LT. The procedure consists in observing the target object (GRB) and other seven stars in the field. Also, known unpolarized sources are observed the same night, in order to minimize the intrinsic polarization introduced by the polarimeter itself and to be able to detect any residual polarization in the GRB emission. A more detailed description of this procedure can be found in Guidorzi et al. (2006) and Steele et al. (2010). The first RINGO2 image was obtained starting at 02:06:43, 243 s after the BAT trigger time, during the brightening phase of the afterglow. The data are consistent with the OT being unpolarized, but unfortunately, due to significant cloud cover, we were able only to determine an upper limit of $<16\%$ polarized (3σ confidence level).

A second observation, centered at 02:58:07.1, 56 minutes after the trigger, was performed under significantly better conditions. We measure the *V*-plus-*R*-band linear polarization of the OT as 3.6%, with a 2σ confidence interval of 0%–6.2%. By randomizing the time sequence of values in the observed trace, we simulate an unpolarized data stream which has exactly the same photometric characteristics as our observations. From many such random realizations, we reject the unpolarized hypothesis at a confidence of 92%.

These values are consistent with the net optical linear polarization estimated in the *R* band a few hours after the burst at the level of $P \sim 1.4\%$, performed by the Calar Alto Observatory equipped with the CAFOS instrument (Gorosabel et al. 2011).

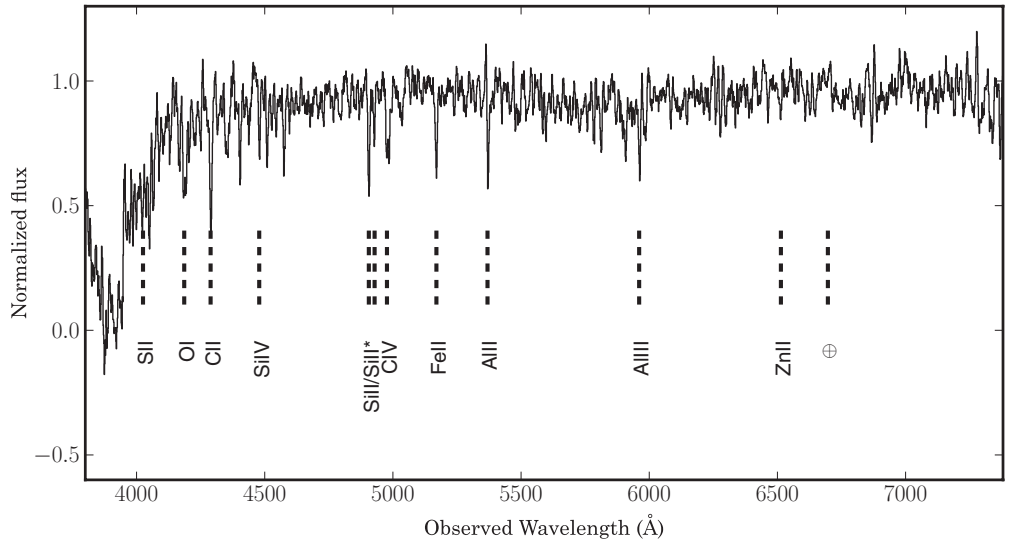

Figure 4. Normalized spectrum of the afterglow of GRB 110205A obtained with the FAST spectrograph ∼3.5 hr after the burst (see Section 2.4 for details). The main absorption features are labeled as well the main atmospheric absorption bands.

Table 2
Best-fit Temporal Parameters

Event	α_1	β_1	$t_{b,1}$	α_2	β_2	$t_{b,2}$
GRB 110205A	-6.13 ± 0.75	1.71 ± 0.28	837^{+51}_{-40}	-0.48 ± 0.22	1.74 ± 0.28	68980
GRB 110213A	-2.08 ± 0.23	1.10 ± 0.24	263^{+13}_{-19}	-2.02 ± 0.34	1.80 ± 0.15	4827

Notes. Best-fit parameters for GRB110205A and GRB110213A using the sum of two Beuermann functions (Beuermann et al. 1999). The multiband fit has been obtained simultaneously in all the observed optical and NIR bands.

The two observations are indicated as red and green arrows in Figure 3.

2.4. Absorption Spectroscopy

We began observing the optical afterglow of GRB 110205A with the FAST spectrograph (Fabricant et al. 1998) mounted on the 1.5 m Tillinghast reflector at Mt. Hopkins Observatory at 5:11 on 2011 February 5. We obtained two 1800 s spectra with the 300 line mm^{-1} grating, covering the wavelength range 3500–7500 Å (Cenko et al. 2011). The data were reduced using standard IRAF routines, including optimal extraction and wavelength calibration relative to a series of HeNeAr calibration lamps. Flux calibration was performed relative to the standard star Feige 34. The resulting co-added, normalized spectrum is shown in Figure 4.

Another spectrum (da Silva et al. 2011) was taken with the Kast spectrograph (Miller & Stone 1993) on the 3 m Shane reflector at Lick Observatory. The reduction procedure was the same as the previous one and the resolution of this spectrum is ∼4 Å in the blue side (around 4500 Å) and ∼10 Å in the red side (around 6500 Å). This spectrum shows a prominent damped Lyα (DLA) absorption system as observed in other GRBs. This feature, in combination with other metal lines (e.g., Fe II, Si II and Si II*, C IV), places the GRB at $z = 2.21442 \pm 0.00044$ (Figure 5). Equivalent widths are estimated and listed in Table 3. The neutral hydrogen column density, estimated by fitting the DLA with a Voigt profile, is $\log(N_{\rm H}) = 21.45 \pm 0.20$, consistent with the one derived by the X-ray analysis, likely implying minimum photoionization of the hydrogen in the circumburst material caused by the burst radiation field (Campana et al. 2010; Watson et al. 2007).

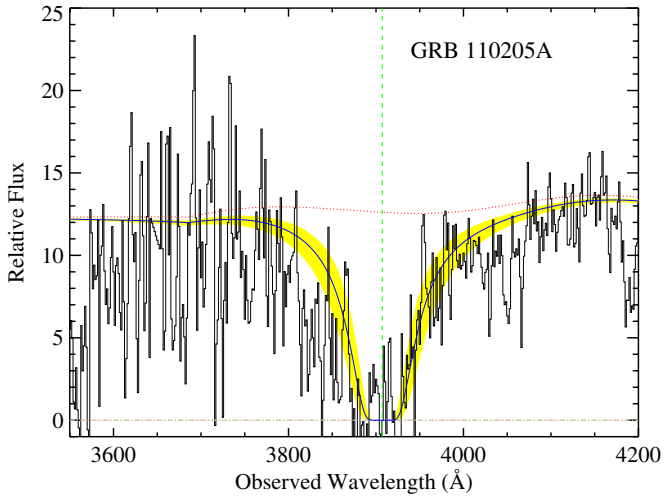

Figure 5. Portion of the spectrum obtained with the Kast spectrograph at Lick Observatory. A DLA absorption system is clearly detected, placing GRB 110205A at $z = 2.22$. The blue line represents the DLA fit, while the shaded area is the 1σ confidence interval. The dotted red line is the continuum fit and the green dashed line identifies the location of the 1216 Å Lyα feature. A Voigt profile fit gives a neutral hydrogen column density of $\log(N_{\rm H}/{\rm cm}^{-2}) = 21.45 \pm 0.23$.

(A color version of this figure is available in the online journal.)

3. GRB 110213A DATA SET

3.1. Space-based Data

GRB 110213A was discovered by *Swift* on February 13 at 05:17:29. The BAT light curve has a typical single-pulse shape, with $T_{90} = 48 \pm 16$ s, estimated in the 15–350 keV energy range.

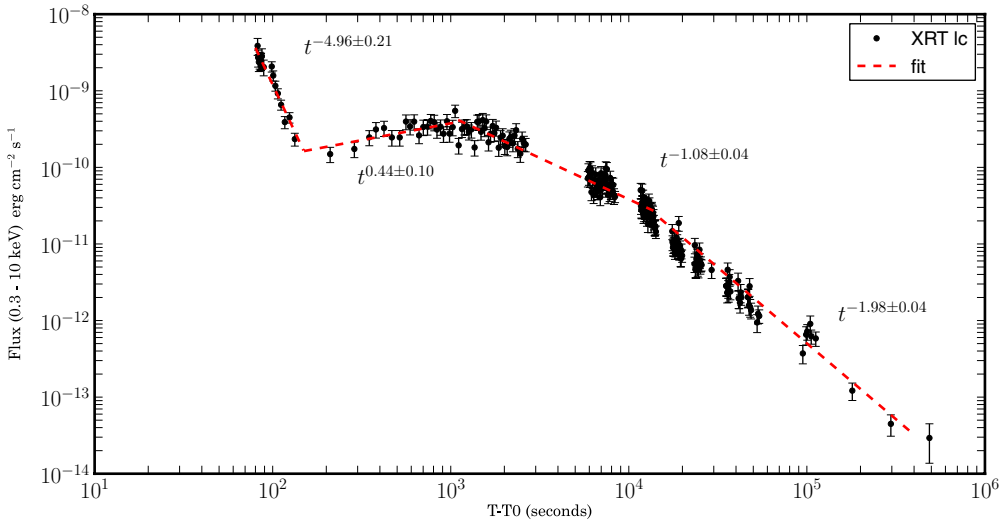

Figure 6. GRB110213A XRT light curve. Dashed lines indicate the different power-law segments obtained fitting the XRT data with single power laws.
(A color version of this figure is available in the online journal.)

Table 3
Absorption Lines in the Afterglow Spectrum of GRB 110205A

λ (Å)	z	Transition	W^a (Å)	$\sigma(W)^b$ (Å)
4030.00	2.21420	S II 1253	<1.10	
4184.83	2.21374	O I 1302	0.69	0.23
4289.89	2.21453	C II 1334	1.31	0.25
4479.97	2.21432	Si IV 1393	<1.09	
4907.11	2.21418	Si II 1526	0.99	0.17
4927.55	2.21432	Si II* 1533	0.54	0.16
4977.05	2.21474	C IV 1548	0.73	0.20
5170.77	2.21408	Fe II 1608	0.86	0.16
5371.76	2.21510	Al II 1670	1.04	0.15
5909.44			2.40	0.59
5962.61	2.21484	Al III 1854	1.18	0.19
6514.62	2.21529	Zn II 2026	<0.51	

Notes.
[a] Equivalent widths are rest-frame values and assume the redshift given in Column 2.
[b] Uncertainties are 2σ statistical values.

The time-averaged spectrum from $T_0 - 31.2$ s to $T_0 + 32.8$ s is best fit by a simple power-law model with a power-law index of $\Gamma_\gamma = 1.83 \pm 0.12$. The fluence in the 15–150 keV band is $5.9 \pm 0.4 \times 10^{-6}$ erg cm^{-2} (D'Elia et al. 2011; Barthelmy et al. 2011; Stratta & D'Elia 2011). The *Konus*-Wind experiment also observed this event reporting similar results (Golenetskii et al. 2011b). Finally, the Gamma-ray Burst Monitor on board the *Fermi* satellite detected the prompt emission of this event (Foley 2011). In the energy range 50–300 keV, the spectrum is well fit by a power-law function with exponential cutoff. The power-law index is $\Gamma_\gamma = -1.44 \pm 0.05$ and $E_{\rm peak} = 98.4^{+8.6}_{-6.9}$ keV. Using the observed fluence value of $1.03 \pm 0.03 \times 10^{-5}$ erg cm^{-2} and $z = 1.46$ (see Section 3.3), we derive an isotropic-equivalent energy of $E_{\rm iso} = 7.2^{+0.1}_{-0.08} \times 10^{52}$ erg.

The *Swift* spacecraft slewed immediately, allowing the XRT to be on target in ∼81 s and to continue observing up to ∼50 ks after the GRB discovery. The XRT enhanced position of the afterglow is R.A.(J2000) = $02^{\rm h}51^{\rm m}51\overset{\rm s}{.}37$, decl.(J2000) = $+49^\circ16'21\overset{''}{.}2$, with an uncertainty of 1.5 arcsec in both directions (Osborne et al. 2011). The XRT light curve can be modeled by different power-law components ($t^{-\alpha}$): initially, at $T < 200$ s, the afterglow steeply decays proportional to $\alpha = 4.96 \pm 0.21$. Subsequently, it flattens and then slowly rises as $\alpha = -0.44 \pm 0.10$ until $T \approx 1500$ s when it starts fading again with $\alpha = 1.08 \pm 0.04$. A final steepening occurs at $T \approx 10^4$ s, after which the X-rays decay as $\alpha = 1.98 \pm 0.04$. There are hints of a possible jet break around ∼1 day post-burst, based on the last observation, which, if valid, would place useful constraints on geometry of the burst emitting region (Figure 6).

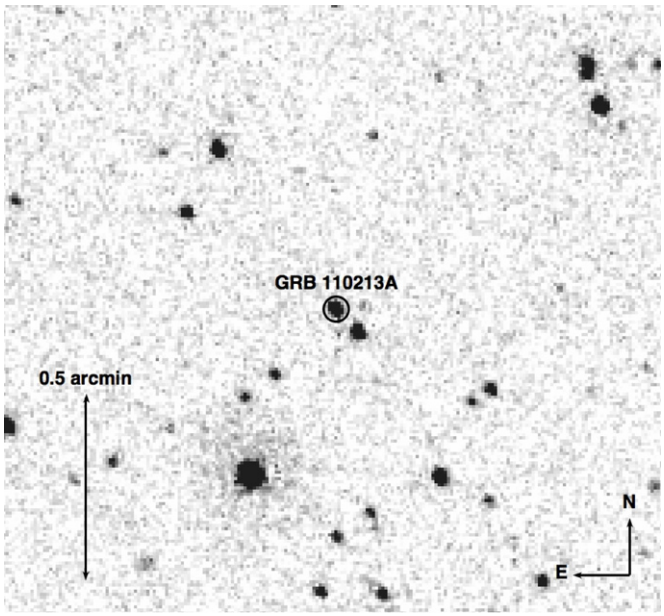

Figure 7. UVOT v band image of GRB 110213A obtained ∼650 s after the trigger.

UVOT started observing ∼100 s after the BAT trigger. The afterglow was detected in the *white*, u, b, v, and $uvw1$ filters at R.A. = $02^{\rm h}51^{\rm m}51\overset{''}{.}40$, decl. = $+49^\circ16'23\overset{''}{.}6$, with an uncertainty of 0.61 arcsec in both directions (Figure 7). In contrast to the early X-ray data, no steep decay is detected at $T \lesssim 300$ s, and instead a rising behavior is present in the *white*-band observations with a power-law index $\alpha = -2.08 \pm 0.23$. Similarly to GRB 110205A, two Beuermann functions fit

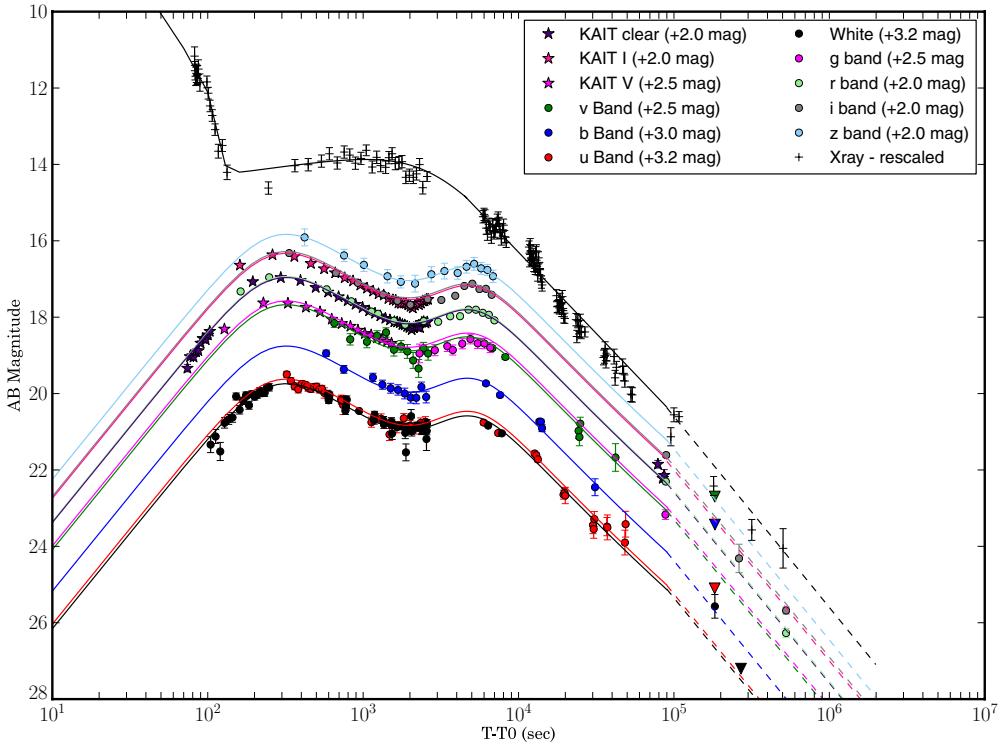

Figure 8. GRB110213A light curve. We represent all the data sets present in this work. All of the magnitudes are transformed into AB systems (Oke & Gunn 1983). We interpret the two peaks as the onset of the afterglow and the continuous energy injection from a long-living central engine.

our data sets simultaneously very well. A peak is detected at $T = 315 \pm 85$ s, after which the optical/UV emission fades as $\alpha = 1.10 \pm 0.24$ until a minimum flux point at around 2000 s, when the emission steeply brightens again with $\alpha = -2.02 \pm 0.34$. After reaching a second peak at $T \approx 4900$ s, the emission decays as $\alpha = 1.80 \pm 0.15$. Unfortunately, due to the afterglow faintness, the UVOT data are sparse, but still cover up to 50 ks after the burst.

3.2. Ground-based Follow-up

The Katzman Automatic Imaging Telescope (KAIT; Filippenko et al. 2001) responded to the trigger within ~70 s after the trigger, observing the afterglow in the unfiltered band followed by V and I. The data were analyzed similarly to the P60 data (Section 2.2) and calibrated using USNO cataloged field stars. The afterglow was detected until $T \approx 3000$ s, during the second rise seen in the UVOT data.

The P60 began observing the optical afterglow of GRB 110213A about 162 s after the trigger and continued sampling the light curve beyond 10^5 s in the four optical filters available, complementing the KAIT observations and confirming the two-peak behavior of the low-energy afterglow emission.

Finally, in order to constrain the late-time ($T > 10^4$ s) behavior we triggered our ToO program at the Gemini-North telescope (PI: B. Cobb), using the GMOS camera (Hook et al. 2004) in imaging mode, performing r' and i' observations six days after the trigger. The object brightness in these bands indicates a possible jet break, in agreement with the X-ray analysis, around $T \approx 1$ day after the burst. A complete summary of our observations can be found in Table 4, and the full light curve is shown in Figure 8 before correcting for Galactic extinction, $E(B - V) = 0.32$.

Table 4
Photometric Observations for GRB 110213A

$T - T_0$ (s)	Filter	Magnitude[a]	1σ Error
	Swift-UVOT		
322	u	15.27	0.07
342	u	15.44	0.08
362	u	15.59	0.09
382	u	15.66	0.09
402	u	15.52	0.08
422	u	15.55	0.08
437	u	15.58	0.03
442	u	15.62	0.09
462	u	15.65	0.09
482	u	15.60	0.08

Notes. [a] UVOT magnitudes are in the natural UVOT photometric system (Vega). See Breeveld et al. (2011) for the most updated zero point and conversion factors.

(This table is available in its entirety in a machine-readable form in the online journal. A portion is shown here for guidance regarding its form and content.)

3.3. Absorption Spectroscopy

We also determined the redshift of this GRB with the Boller and Chivens Spectrograph mounted on the Steward 2.3 m Bok telescope on Kitt Peak, AZ. Based on several metal lines, including Fe II, Fe II*, Ni II, and Al II, we found $z = 1.4607 \pm 0.0001$ (see Figure 9). Equivalent widths for some of these features are listed in Table 5.

4. RESULTS

GRB 110205A and GRB 110213A present well-sampled light curves from high energy to optical and NIR bands, covering a large timeline. We now frame the observed behavior

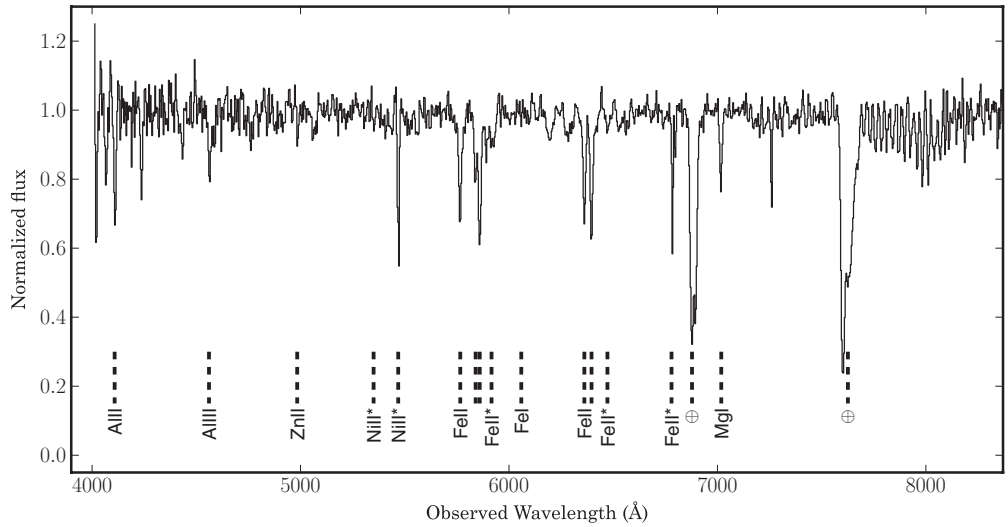

Figure 9. Normalized spectrum of the afterglow of GRB 110213A obtained with the Bok spectrograph. The main absorption features are labeled, as are the telluric lines.

Table 5
Absorption Lines in the Afterglow Spectrum of GRB 110213A

λ (Å)	z	Transition	W^a (Å)	$\sigma(W)^b$ (Å)
4112.10	1.46233	Al II 1670	1.96	0.33
4238.78			2.39	0.68
4566.75	1.46311	Al III 1854	1.73	0.21
4984.60	1.45934	Zn II 2026	<0.60	
5310.17			2.77	0.29
5354.79	1.46197	Ni II* 2175	1.16	0.11
5404.37			3.12	0.27
5433.04			2.27	0.27
5471.65	1.46138	Ni II* 2223	1.82	0.11
5767.82	1.46067	Fe II 2344	3.51	0.09
5859.36			13.31	0.22
5893.38	1.45967	Fe II* 2396a	4.54	0.09
5918.62	1.46096	Fe II* 2405	6.89	0.09
6237.86			80.12	0.22
5998.19			6.16	0.22
6062.10	1.46126	Fe I 2463	1.01	0.09
6089.69			2.14	0.21
6135.74			1.29	0.21
6196.43			4.30	0.21
6286.07			5.45	0.21
6363.63	1.46080	Fe II 2586	2.73	0.08
6397.78	1.46068	Fe II 2600	3.31	0.08
6475.33	1.46116	Fe II* 2631	1.76	0.08
6530.68			3.51	0.20
6562.87			4.03	0.20
6786.08	1.46229	Fe II* 2756	1.20	0.07
7018.68	1.46010	Mg I 2853	1.81	0.19

Notes.
[a] Equivalent widths are rest-frame values and assume the redshift given in Column 2.
[b] Uncertainties are 2σ statistical values.

of the afterglow emission within the *internal–external* shock scenario, emphasizing the analogies and differences as well as the limitations of the current follow-up efforts. The data allow constraining statements about the emission mechanisms and the interaction of the afterglow with the surrounding material. Throughout the following we will use the usual notation where $F(\nu, t) \propto \nu^{-\beta} f(t)$, where $f(t)$ is a Beuermann function or a simple power-law model and β the spectral index.

4.1. GRB 110205A

GRB 110205A represents an important laboratory in which to test the standard *internal–external* shock model. It presents several characteristics of the "typical" GRB prompt emission as well as of the afterglow component. We can divide the detected emission into three main parts: (1) the prompt emission ($T \lesssim 400$ s), which has been observed by all three instruments on board the *Swift* satellite; (2) the optical peak region ($400\,\mathrm{s} \lesssim T \lesssim 10^3$ s after the burst); and (3) the late-time phase ($T \gtrsim 10^3$ s).

4.1.1. Prompt Phase

The prompt emission of GRB 110205A, as detected by the BAT instrument, is composed of a series of peaks as seen in several other long GRBs. The observed fluence, $f = 2.7^{+0.7}_{-0.4} \times 10^{-5}$ erg cm^{-2}, is on the higher end of the *Swift*-GRBs fluence distribution at similar redshift as estimated recently by Mészáros et al. (2011) and the isotropic energy emitted, $E_{\rm iso}$, places GRB 110205A well within the 3σ confidence level of the $E_p - E_{\rm iso}$ correlation for long GRBs (Amati et al. 2008).

Furthermore, similarly to other cases (e.g., GRB 080319B; Racusin et al. 2008), the XRT and UVOT instruments were able to begin observing before the end of the prompt phase. The multiple peak nature of the prompt emission is consistent with each peak being produced by internal shocks due to the collision of different shock fronts. In Figure 10, we overplot the UVOT *white*-band light curve in comparison with the XRT and the BAT signal during the first 400 s after the burst trigger. A bright and very sharp peak at ∼220 s ($\Delta t/t \lesssim 1$) is also detected in the UVOT band, and it is consistent with an internal dissipation process (Ioka et al. 2005).

Over the entire prompt phase, the X-ray and gamma-ray emissions have a similar average photon index ($\Gamma_{\rm ave} \approx 1.59$) derived from the BAT and *Suzaku* data. Rescaling the hard X-ray emission into the XRT energy range, the light curves align with each other as can be seen clearly in Figure 1.

Furthermore, at the most prominent peak in the BAT data, at $T \sim 220$ s after burst, the X-ray spectral index is $\beta \sim -0.12 \pm 0.04$. In Figure 11, we present the SED constructed using the X-ray data and the *white* filter observation at $T = 220$ s. A single power-law extrapolation from the high-energy band overpredicts the *white*-band observation by a factor of ∼2,

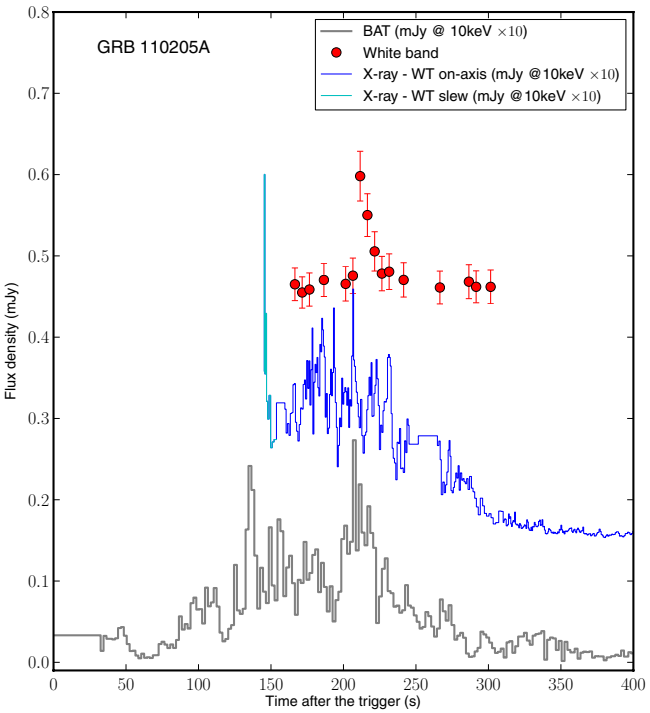

Figure 10. Early-time light curve comparison. The BAT flux density (gray histogram, 1 s bin) has been extrapolated in the XRT bandpass (0.3–10 keV). Red points are UVOT *white*-band detections (5 s bin), while the cyan and blue points are XRT window-timing mode detections (0.5 s bin) during and after the slewing procedure, respectively. There is a hint of correlation between the optical and the high-energy bands, probably indicative of a similar emission mechanism during the prompt phase. The three curves have been shifted along the ordinate to facilitate this comparison.

(A color version of this figure is available in the online journal.)

indicating that the X-ray and the optical emission may likely belong to the same segment of the SED and are produced by the same electron population (see also Rossi et al. 2011; Shen & Zhang 2009; Vestrand et al. 2006 for similar studies). The discrepancy in the observed low-energy flux is not surprising, since the broadband filter extends blueward at 2000 Å and redward up to 6000 Å. Part of the flux, then, is suppressed by the presence of the Lyα break which is redshifted at 3912 Å ($z = 2.214$).

A break between the X-ray and the optical bands (imposing ν^{β} with $\beta = 1/3$; dash-dotted line in the figure) would fit the data better, but would be inconsistent with the SED at later time. In fact, as a comparison, we present a multiband SED constructed at $T \approx 400$ s and $T \approx 520$ s after the burst. In these cases a break will be required in order to account for the change in the X-ray spectral index as seen in other similar cases (Rossi et al. 2011), probably due to one of the characteristic synchrotron frequencies. The following fast decline observed in the X-ray regime is probably due to the tail of the prompt emission and it is governed by the high-latitude effect (hereafter HLE; Kumar & Panaitescu 2000), for which emission from different viewing angles reaches the observer with different delays due to the light propagation effect (see Racusin et al. 2009, and references within for a complete taxonomy of the X-ray light curves). At the same time ($350\,\mathrm{s} \lesssim T \lesssim 600\,\mathrm{s}$), the X-ray spectrum undergoes a hard-to-soft evolution which has been characteristic of a large number of GRBs. In the HLE, the temporal and spectral indices are correlated such that $\alpha = 2 + \beta$ (Kumar & Panaitescu 2000). In the case of GRB 110205A, this is not satisfied because the derived values are $\alpha_X = 5.39$ and $\beta_X \approx 0.5$, but, as shown in Zhang et al. (2006), shifting the time zero point (t_0) of the afterglow can reconcile the observation with the theory without ruling out the curvature-effect interpretation. Assuming that the afterglow starts at $t_0 \approx 200$ s a new fit of the X-ray light curve gives a temporal index of $\alpha_X = 2.70 \pm 0.10$, in agreement with the expected value from the curvature effect ($\alpha_{\mathrm{theo}} = 2.5$).

4.1.2. Optical Peak Time

After 600 s, the X-ray afterglow declines with a temporal index $\alpha_X = 1.65$, likely the signature of a *forward*-shock dominated emission taking place. Flaring activity is also detected at this time, which is not unusual for the X-ray emission (Margutti et al. 2011; Chincarini et al. 2010; Gao 2009; Marshall et al. 2011).

At the same time, however, the optical emission undergoes a steep increase in flux: assuming that this rising began at the time of the trigger ($t_0 = t_{\mathrm{trigger}}$) the optical flux increases

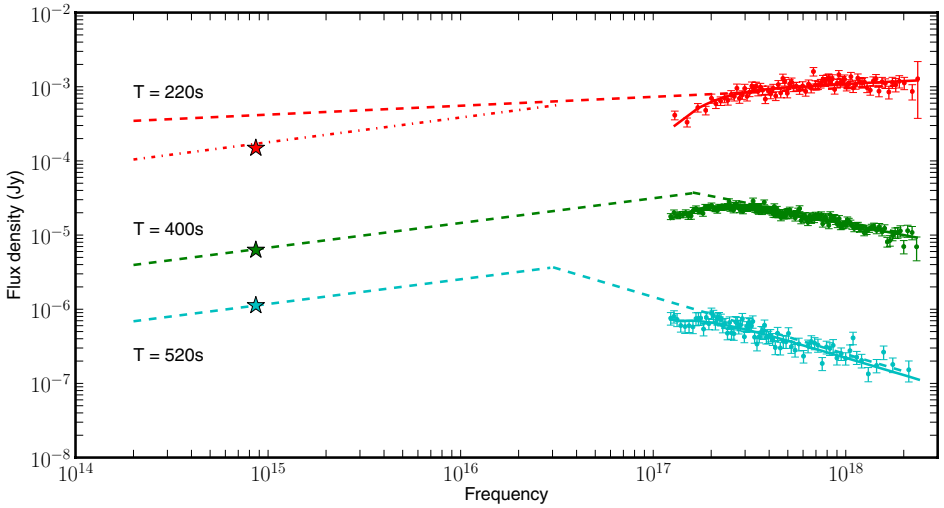

Figure 11. Spectral energy distribution constructed using the XRT and the UVOT *white*-band data at the time of the optical peak ($T \approx 220$ s), at $T \approx 400$ s, and at $T \approx 520$ s, when the high-latitude effect likely dominates the observed emission. Fitting the SED at the peak with a broken power law, as shown by the dash-dotted line (imposing a spectral index $\beta = 1/3$ at $\nu_{\mathrm{opt}} < \nu < \nu_X$), implies a spectral break which is inconsistent with the spectral evolution at later times. The most likely scenario is that the *white*-band detection is affected by attenuation due to the DLA and the broadband transmission curve of the UVOT filter.

(A color version of this figure is available in the online journal.)

as $t^{-\alpha_{\rm opt}}$, with $\alpha_{\rm opt} = -6.13 \pm 0.75$ (χ^2/dof = 1.29) until $t_{\rm peak} \approx 985$ s. As discussed in other cases (Liang et al. 2006; Quimby et al. 2006; Lazzati & Begelman 2006; Kobayashi et al. 2007; Rossi et al. 2011) the power-law index is very sensitive to the choice of t_0. In particular, the rise slope is estimated by $d \ln F_\nu(t)/d \ln (t - t_0')$, where $t_0' = t_{\rm trigger} + t'$, instead of the usual $d \ln F_\nu(t)/d \ln (t - t_{\rm trigger})$. Assuming that the optical emission started *after* the actual trigger time ($t' > 0$), for example, at the time of the optical brightest point in the *white* band (see the previous section), the fit slightly improves (χ^2/dof = 1.19) and a shallower rising index of $\alpha_{\rm opt} = -3.96 \pm 0.86$ is obtained. This value is consistent with a reverse-shock theoretical prediction (e.g., $\alpha_{\rm theo} = -5$; Zhang et al. 2003). Instead, assuming an *earlier* emission ($t' < 0$) does not produce a better fit and, as result, implies an even steeper power-law index. In this last scenario, considering also the absence of a clear precursor in the gamma-ray band, it would be difficult to explain such emission in the optical before the hard X-ray.

Overall, this peculiar behavior, similar in all the observed bands from UV to optical, can originate from a *forward* shock or, as suggested in a few other cases, from the *reverse* shock. In both cases, assuming the synchrotron self-absorption frequency is well below the optical band, $\nu_a < \nu_{\rm opt}$, the thickness of the shell and the density profile ("homogenous ISM" (interstellar medium) or "wind-like" medium) affect the rate at which the light curve rises.

For instance, we are aware of no theoretical model that predicts such steep rising during the forward shock, while if the rising is due to the onset of the afterglow it is important to determine if we are in the "thin-shell" or "thick-shell" regime (e.g., Kobayashi 2000; Sari et al. 1998). For a "thin shell," in a constant ISM, the temporal index is either $\alpha = -2$ ($\nu_c < \nu_{\rm opt}$) or $\alpha = -3$ ($\nu_c > \nu_{\rm opt}$; Zhang et al. 2003). A "thick shell" would imply a much shallower rise in flux before the peak. In the case of a wind-like medium we expect a much shallower rise ($\alpha = -1/2$; Kobayashi & Zhang 2003). Therefore, it is very unlikely that either a forward-shock emission or the passage of a synchrotron characteristic frequency in the observed band could reproduce the observed early-time optical light curve.

A reverse shock can produce the observed rising, but again it is critical to determine the regime in which the emission takes place (Zhang et al. 2003). First of all, the $\alpha \approx -5$ can only exist in a thin-shell regime, since the thick regime has a shallower rising $\alpha = -1/2$. We define $\Re_\nu = \frac{\nu_R}{\nu_{m,r}(t)}$, the ratio between the optical R-band frequency and the typical synchrotron frequency ν_m. For the reverse shock, $\Re_\nu > 1$ ($\nu_{m,r} < \nu_R$, thin shell, reverse shock). We can calculate $\nu_{m,r}$ and $\nu_{c,r}$ at the peak, 985 s after the burst, since we expect $\nu_{c,r}(t_{\rm peak}) = \nu_{c,f}(t_{\rm peak})$, where the subscripts indicate the reverse and forward shock, respectively. From Equation (1) of Zhang et al. (2003), we obtained that the critical Lorentz factor is $\gamma_c \approx 550$, while the initial Lorentz factor can be estimated from the Lorentz factor at the peak time, $\gamma_{\rm peak}$ (Mészáros 2006):

$$\gamma_0 = 2 \times \gamma_{\rm peak} = 2 \times \left(\frac{3(1+z)^3 E}{32\pi n m_p c^5 t_p^3}\right)^{1/8} \approx 200 \left(\frac{E}{4\times10^{53}\,{\rm erg}}\right)^{1/8} n^{-1/8} \left(\frac{1+z}{3.22}\right)^{3/8} \left(\frac{t_p}{985\,{\rm s}}\right)^{-3/8}.$$

For GRB 110205A, we see that $\gamma_0 < \gamma_c$, confirming that our assumption of a thin-shell regime is indeed correct. At the time of the peak: $\nu_{c,r} = 2.31 \times 10^{16}$ Hz (for $\epsilon_B = 10^{-2}$) and $\nu_{m,f} = 1.2 \times 10^{15}$. Finally, using $\nu_{m,r} \sim \gamma_0^{-2} \nu_{m,f}$ we can see that we are likely in $\nu_{m,r} < \nu_R < \nu_c \lesssim \nu_X$. Another point in favor of a thin-shell regime is the burst duration. In fact, in this case the deceleration time t_γ is longer than the duration of the burst T_{90}, while for a thick shell we would expect a much shorter timescale.

If the optical band is located below the typical frequency of the *forward* shock at the deceleration time ($\nu_{\rm opt} < \nu_{m,f}$), the optical bandpass is dominated by the *reverse*-shock emission. Although this interpretation seems favorable in explaining the temporal behavior, in this scenario the light curve should manifest the passage of $\nu_{m,f}$ in the observed bands (see Figure 1 in Kobayashi & Zhang 2003), and it is not consistent with the observations. Then, the optical band should be roughly around or above $\nu_{m,f}$ at the deceleration time. We can estimate this from

$$\nu_{m,f} = (6 \times 10^{15}\,{\rm Hz})(1+z)^{1/2} E_{52}^{1/2} \epsilon_e^2 \epsilon_B^{1/2} (t/1\,{\rm day})^{-3/2},$$

for which, for the observed value of $E_{\rm iso}$, z, and time of the peak, and using typical values for ϵ_e and ϵ_B, we estimate $\nu_{m,f} \approx 3 \times 10^{14}$ Hz. Under this condition, the onset of the afterglow is expected to be a single peak as observed in other cases (Mundell et al. 2007a, 2007b). At the peak time, the contributions of the two shock emissions to the optical band are comparable, provided that the microscopic parameters are similar in the two shocked regions. The rapid rise is due to the bright reverse-shock emission which masks the onset of the forward-shock emission, and it implies a weakly magnetized outflow from the central engine (Fan et al. 2002; Zhang et al. 2003; Kumar & Panaitescu 2003; Gomboc et al. 2008).

It is worthwhile to note that the peak flux density in V band is 3 mJy, as observed by UVOT, and it is consistent with the sample of Panaitescu & Vestrand (2011) (see also Vestrand et al. 2006) for "peaky" afterglows, where, for a constant-ISM model and after a steep rise due to the fireball deceleration, the optical emission reaches a flux density of ~4 mJy (see Figure 12). After the onset of deceleration the afterglow is forward-shock dominated and evolves with the usual single power-law decay (except for the presence of a possible jet break).

4.1.3. Late-time Behavior

After the reverse shock has passed through the GRB ejecta, the synchrotron emission produced by an external shock interacting with the ISM becomes the dominant emission mechanism. The emission from the reverse shock decays as fast as t^{-2}, so we expect a power-law decline as $t^{-\alpha}$, with $\alpha = (3p-2)/4$ (for $\nu_{\rm opt} < \nu_c$) or $\alpha = 3(p-1)/4$ (for $\nu_m < \nu_{\rm opt} < \nu_c$). The late-time optical–NIR decay indices are $\alpha_{\rm opt} = 1.74 \pm 0.28$, in agreement with the X-ray decay index $\alpha_X = 1.65 \pm 0.05$, suggesting a forward shock producing the emission from the optical to the X-ray. Assuming that the X-ray afterglow emission is dominated by forward shock, we estimated $p = 2.90$ ($\alpha_X = (3p-2)/4$), where p is the index of the power-law distribution of random electrons accelerated at the shock (Zhang et al. 2003).

The observations performed by the RINGO2 polarimeter exclude the zero-polarization hypothesis at 92% confidence level, supporting the reverse plus forward-shock scenario, in which the afterglow is mainly dominated by the forward shock. Nevertheless, such low polarization as $P = 3.6\%$ can be the result of several scenarios, like a structured jet (Rossi et al. 2004), the alignment of the magnetic field over causally

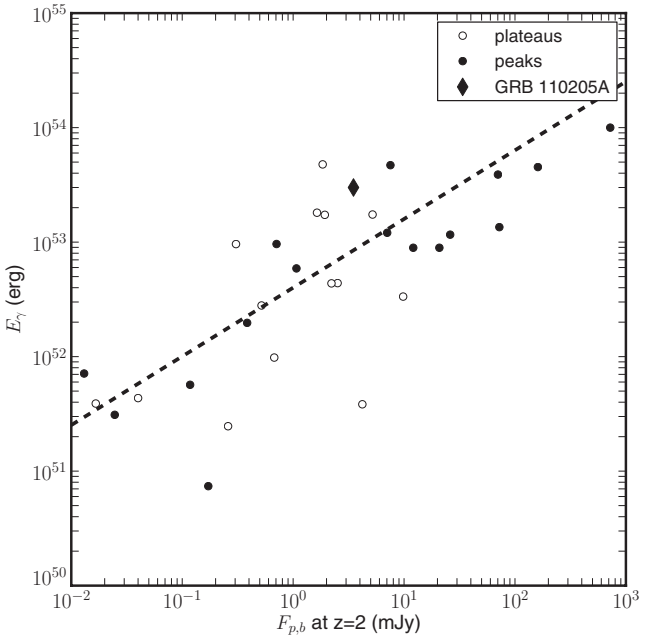

Figure 12. Figure adopted from Panaitescu & Vestrand (2011). The abscissa represents the optical flux at the observed peak time, F_p (or at the end of an extended plateau phase, T_b). GRB 110205A is plotted as a filled diamond and presents a peak luminosity compared to other "peaky" afterglow cases (filled circles) or GRBs that present plateau phases (open circles). The dashed line represents the correlation between these fluxes and the isotropic-equivalent energy released (E_γ). As mentioned by these authors the rising in the light curve may be due to a deceleration of the fireball which implies a large release of energy in a short amount of time.

connected regions (Gruzinov & Waxman 1999), or even a large-scale magnetic field in the ambient medium (Granot & Königl 2003). This result is also consistent with many other GRB polarization measurements (see Covino et al. 2004; Mundell et al. 2010, and references within for the state of the art of polarization studies).

4.1.4. Absorption Spectrum

We also observed the afterglow of GRB 110205A with the Kast spectrograph on the 3 m Shane reflector at Lick Observatory. Despite the fact that only a few absorption features could be identified, a clear indication of high neutral hydrogen in the host galaxy of this GRB comes from the detection of a DLA absorption system. A fit of the broad absorption profile indicates a value of $\log(N_{\rm H}/{\rm cm}^{-2}) = 21.45 \pm 0.2$ (Figure 5), similar to the value obtained from the X-ray data, perhaps indicating minimal photoionization of the surrounding medium from the GRB itself (see also Campana et al. 2010; Watson et al. 2007).

4.2. GRB 110213A

Optical data for GRB 110213A were obtained only after the prompt emission had ended. Nevertheless, our group was able to observe this event from several different facilities, such as the P60 and KAIT, providing much coverage of the afterglow phase.

4.2.1. Prompt Phase

The prompt emission exhibits a single-peak profile and a soft spectrum. Using $E_{\rm peak}$ and $E_{\rm iso}$ derived by *Swift* and other space facilities, GRB 110213A does not differ from other long-soft GRBs; thus, not surprisingly, it also obeys the Amati relation for long GRBs (Amati et al. 2008).

4.2.2. X-Ray Light Curve

In the time between the beginning of the observations with XRT/UVOT and KAIT, the X-ray fades steeply with $\alpha_X = 4.96 \pm 0.21$. This early steep declining phase, as for GRB 110205A, is consistent with being the tail of the prompt emission and it is governed by the curvature effect. In particular, the spectral index and the temporal index are correlated by $\alpha = 2 + \beta$. Using the estimated photon index from the first 150 s ($\Gamma_X = 5.10 \pm 0.78$), we obtain $\alpha = 6.10 \pm 0.78$, which is consistent with the observed steep decay at a 1σ confidence level. At $T > 150$ s the X-ray emission brightens with $\alpha_X = -0.44 \pm 0.10$ up to $\sim$1500 s and then follows a shallow decay until 10^4 s with $\alpha_X = 1.08 \pm 0.04$.

Using the spectral index $\beta_X = 1.12 \pm 0.12$, we can determine that the behavior of GRB 110213A is consistent with the forward-shock scenario where the central engine is ejecting material in a slow-cooling regime in a homogenous ISM. Using the closure relation $\alpha = (q-2)/2 + (2+q)\beta/2$ we obtain $\alpha = -0.44$, where q is defined as $q = 2(\alpha + 1 - \beta)/(1+\beta)$, for $\nu > \nu_c, \nu_m$ and characterizes the central engine behavior (where we have $q < 1$ for an adiabatic fireball modified by continued injection as presented in Zhang et al. 2006). The peak represents the cessation of the energy injection, after which the normal adiabatic expansion of the fireball is expected. We derive for 10^4 s $\lesssim t \lesssim 10^6$ s a decay index of $\alpha_X = 1.98 \pm 0.07$. In summary, the overall X-ray behavior of GRB 110213A is consistent with that of other GRBs in the *Swift* sample (e.g., Evans et al. 2009).

4.2.3. Optical Behavior—$T < 2000$ s

KAIT observations of GRB 110213A indicate a rising afterglow with $\alpha = -2.08 \pm 0.23$ from $T = 70$ s until $T = 321$ s. From the sample of Oates et al. (2011, 2009), UVOT observed six GRBs with rising afterglows in the first 500 s. GRB 110213A has a very similar case. What can be the cause of the peak at 321 s? Several possibilities need to be tested: (1) the passage of one of the characteristic frequencies (e.g., ν_m); (2) a reverse shock, as seen in GRB 110205A; (3) a decreasing extinction with time; and (4) the onset of the forward shock.

The characteristic frequency ν_m that produces a peak in the light curve has a time dependence of $\nu_{m,f} \propto t^{-3/2}$ and should produce a chromatic break, meaning that the peak should be earlier in the bluer bands than the redder ones. During the rising part only KAIT, UVOT *white*, and P60 r'-band observations are available, so it is a challenging task to assess this chromaticity due to the gaps in the light curve. Nevertheless, during the passage of ν_m the spectral index changes from $\nu^{1/3}$ (for $\nu < \nu_m$) to $\nu^{-(p-1)/2}$ (for $\nu_m < \nu < \nu_c$). Based on this we can estimate that the color change between the UVOT *white* filter and P60 r' observation before and after the peak should be 0.68 mag. Instead, we measure a color difference of 0.15 ± 0.10 (after correcting for Galactic extinction). Furthermore, if we assume a constant density medium, $\nu_{m,f}$ can be calculated as

$$\nu_{m,f} = (6 \times 10^{15}\ {\rm Hz})(1+z)^{1/2} E_{52}^{1/2} \epsilon_e^2 \epsilon_B^{1/2} (t/1\ {\rm day})^{-3/2}.$$

For $z = 1.46$, $E_{52} = 7.2$, and $t = 0.004$ day, and assuming that $\nu_{m,f}$ is already below the r' band we obtain the constraint $\epsilon_e^2 \epsilon_B^{1/2} < 5.6 \times 10^{-6}$, consistent with other GRBs in the samples of Oates et al. (2009) and Panaitescu & Kumar (2002), in which the values of $\epsilon_e^2 \epsilon_B^{1/2}$ range from 3×10^{-3} to 2×10^{-7}. Therefore, we can exclude that the peak observed is due to the passage of

ν_m. As suggested by some authors (Klotz et al. 2008; Rykoff et al. 2004), if there were a significant amount of extinction at the beginning of the afterglow phase the resulting light curve would be dim and reddened. Then, because of the dust-destruction effect, it would rise faster in the blue filters than in the red ones. Of course this effect strongly depends on the GRB environment, but the KAIT, P60, and UVOT *white* observations, which all trace the rising phase, show similar α index, from the blue bands (UVOT *white*) to the red (P60 r'). So we can also exclude that this effect is the dominant cause of the rising at early time.

The rising in the light curve at $T < 321$ s is more likely due to the onset of the forward shock. Unlike GRB 110205A, the rather slow rise does not require the domination of the reverse-shock emission at early times. The post-peak decay $\alpha = 1.10 \pm 0.24$ is also much shallower than the typical reverse-shock index ($\alpha = 2$). The forward-shock emission masks the reverse-shock emission when the typical frequency of the forward shock is below the optical band or when the magnetization of the ejecta is very high ($\sigma = B^2/4\pi\gamma\rho c^2$ is about unity or larger) and the magnetic pressure suppresses the reverse-shock emission (Giannios et al. 2008). The observed $\alpha = -2.08$ is consistent with the expected $\alpha = -2$ for $\nu_c < \nu_{\rm opt}$ in a "thin"-shell scenario for a homogeneous ISM.

Finally, for a constant density medium, we can use the peak time to determine the Lorentz factor at that time using the formalism of Sari & Piran (1999), like in similar other cases (Molinari et al. 2007). We obtain $\Gamma(t_{\rm peak}) \approx 139(\eta n_0)^{-1/8}$, where η and n_0 are the radiative efficiency and the density of the shocked medium, respectively. Usually, the initial Lorentz factor is twice the value at peak, allowing us to estimate the deceleration radius of the fireball to be $R_{\rm dec} \approx 2.27 \times 10^{17}$ cm. The Lorentz factor and the deceleration radius are also consistent with the theoretical values predicted by Rees & Meszaros (1992), as well as with the sample of Oates et al. (2009).

4.2.4. Optical Behavior—$T > 2000$ s

A second peak at $t_{\rm peak} = 4975 \pm 545$ s is detected by several facilities, but is most prominent in data from the Palomar P60 and, in the decaying phase, the UVOT. Again, as previously, this feature can be due to one of the characteristic frequencies passing in the optical bands (in particular, at such late time, the synchrotron characteristic frequency ν_c). Another possibility is that the emission is from the newly injected material in the blast wave (energy injection model).

In the case of synchrotron origin, we calculated the optical spectral indices before and after the peak at $t_{\rm peak} = 4975$ s. We obtain $\beta_{o,\rm pre} = 1.12 \pm 0.24$ and $\beta_{o,\rm post} = 1.22 \pm 0.18$. These values are consistent with each other within 1σ, indicating that $\nu_c < \nu_{z'}$ or $\nu_c > \nu_{\rm white}$ at $t = t_{\rm peak}$.

Also, the passage of a characteristic frequency during our observation would imply a chromatic feature, mainly a different peak time at different frequencies. We tested this possibility assuming, for example, that the peak in the z' band at $t_{z',p} = 4975$ s is due to the characteristic synchrotron frequency. Using the scaling law in Sari et al. (1998), we estimated that the peak would have crossed the UVOT u band at

$$t_{u,p} = t_{z',p} \times \left(\frac{\nu_{c,z'}}{\nu_{c,u}}\right)^2 = 743\ {\rm s}.$$

From Figure 8 it is evident that this is not the case.

One more possibility which would produce a "bump" in the light curve is the interaction of the fireball with moderate overdensity regions in the ambient medium (Lazzati et al. 2002), although, in this case, the light curve returns to the original power-law decay after the fireball has passed through these overdensity regions, which is inconsistent with our observations.

Instead, the most likely scenario, in agreement with the X-ray analysis, is that the rise and the following decays at late time are due to the re-injected material from the central engine into the ISM. At late time, in this case, we expect a somewhat steeper decay than the usual adiabatic regime ($\alpha = (2-3p)/4$). The decay index from the optical multiband fit is consistent with $\alpha = 1.80 \pm 0.15$, in agreement with the X-ray emission, whereas the adiabatic regime gives $\alpha = 1.37$ assuming a typical value of $p = 2.5$. Our assumption of a re-injection phase better explains our late-time data.

Finally, using our Gemini ToO program we observed the afterglow in the r' and i' bands around 6 days after the burst. The object is detected, but significantly below the extrapolation of the light curve from the early data. This suggests the presence of a jet break after 1 day, placing a constraint on the opening angle of $\theta_{\rm jet} \gtrsim 5^\circ$, and assuming the afterglow is the dominant source of radiation with a negligible contribution from the host galaxy.

4.2.5. Absorption Spectrum

The redshift of $z = 1.46$, determined using the Bok telescope, allows the identification of UV rest-frame lines of low-ionization species. In particular, fine-structure transitions, like Ni II* and Fe II*, are indicative of UV pumping as the principal excitation mechanism in the vicinity of the GRB. No neutral hydrogen estimate is possible, again, due to the low-redshift nature of this GRB.

5. CONCLUSION

We observed GRB 110205A and GRB 110213A, discovered by the *Swift* satellite, with a broad range of follow-up facilities. The combination of our data sets and the publicly available *Swift* data covers more than six orders of magnitude in time.

GRB 110205A represents one of the best cases in which it has been possible to determine the contribution of the *reverse* shock. While the UVOT and XRT data trace very well the prompt phase, they also allow the characterization of a fast rising ($\alpha = -6.13 \pm 0.75$) due to the reverse shock. After the peak at $T \approx 985$ s, the behavior is consistent with a combination of reverse and forward shocks, providing a shallower decay than the one expected for a pure *reverse* shock. A polarization measurement around 9 minutes after the burst provides only an upper limit (limiting polarization of $< 16\%$), with a 2σ linear polarization detection obtained around 1 hr post-burst ($P = 3.6\%$). This value is in agreement with other estimates ($P = 1.4\%$; Gorosabel et al. 2011). Unfortunately, in the absence of polarization variability information, we were unable to constrain the nature of the GRB environment or of the jet. Nevertheless, the reverse-shock emission dominates over the optical band and masks the forward-shock emission at early times and it implies a weakly magnetized fireball.

Ground-based optical spectra reveal the presence of a strong DLA absorption system at $z = 2.22$, produced by a neutral hydrogen column density of $\log(N_{\rm H}/{\rm cm}^{-2} = 21.45 \pm 0.2)$. This is not surprising, but it is interestingly similar to the value obtained from the X-ray data, implying minimal photoionization of the surrounding medium from the GRB itself.

In contrast, GRB 110213A presents a clear indication of a refreshed shock, most likely produced by long-lived activity of

the central engine. In the X-ray, the plateau phase is followed by the typical adiabatic behavior and by a steep decaying phase consistent with post-injection emission. In the optical, using seven bands (from the UVOT-*white* to the P60 z' filters), the afterglow presents two peaks due to the onset of the forward shock and to the interaction of the injected material with the ISM. Other interpretations, such as the passage of the characteristic synchrotron frequencies in the observed bands, are ruled out since no chromatic features are present in our data sets. In the case of GRB 110213A, then, the forward-shock emission masks the reverse-shock emission, which means that the typical frequency of the forward shock is lower than the optical band or that the magnetic pressure is suppressing the reverse shock.

Using our late-time Gemini observations, we were also able to detect the afterglow well beyond the capabilities of our small robotic telescopes. These observations provide some constraints on the jet opening angle of the GRB emission. In particular, we can place a lower limit of $\theta_{\rm jet} \gtrsim 5^{\circ}$.

The importance of robotic facilities, multiband observations, and spectroscopic follow-up reinforces the notion that a large array of facilities are needed in short order to interpret the complex early-time behavior of GRBs. Future implementations, in particular using near-infrared cameras mounted on larger facilities, will allow the characterization of even higher redshift events, and will help test the dust properties of their environments (e.g., Farah et al. 2010). The synergy between ground-based and new-generation space-based observatories will provide the best simultaneous coverage of these kinds of events, providing a complete description of the GRB phenomenon and GRB progenitors up to redshifts $z \gtrsim 9$.

A.C. acknowledges the anonymous referee for the valuable comments in order to improve the quality of this work. The Gemini data, acquired under the program ID GN-20011A-Q-4, are based on observations obtained at the Gemini Observatory, which is operated by the Association of Universities for Research in Astronomy, Inc., under a cooperative agreement with the NSF on behalf of the Gemini partnership: the National Science Foundation (United States), the Science and Technology Facilities Council (United Kingdom), the National Research Council (Canada), CONICYT (Chile), the Australian Research Council (Australia), Ministério da Ciência e Tecnologia (Brazil), and Ministerio de Ciencia, Tecnología e Innovación Productiva (Argentina). A.V.F., S.B.C., and W.L. acknowledge generous financial assistance from Gary & Cynthia Bengier, the Richard & Rhoda Goldman Fund, NASA/*Swift* grants NNX10AI21G and GO-7100028, the TABASGO Foundation, and NSF grant AST-0908886. KAIT and its ongoing operation were made possible by donations from Sun Microsystems, Inc., the Hewlett-Packard Company, AutoScope Corporation, Lick Observatory, the NSF, the University of California, the Sylvia & Jim Katzman Foundation, and the TABASGO Foundation. A.C. thanks C. Guidorzi and D. A. Kann for the useful discussion and comments.

REFERENCES

Abazajian, K. N., Adelman-McCarthy, J. K., Agüeros, M. A., et al. 2009, ApJS, 182, 543
Amati, L., Guidorzi, C., Frontera, F., et al. 2008, MNRAS, 391, 577
Barthelmy, S. D., Barbier, L. M., Cummings, J. R., et al. 2005, Space Sci. Rev., 120, 143
Barthelmy, S. D., Barbier, L. M., Cummings, J. R., et al. 2011, GCN Circ., 11714, 1
Beardmore, A. P., Baumgartner, W. H., Burrows, D. N., Chester, M. M., & Gelbord, J. M. 2011a, GCN Circ., 11629, 1
Beardmore, A. P., Evans, P. A., Goad, M. R., & Osborne, J. P. 2011b, GCN Circ., 11639, 1
Bertin, E., & Arnouts, S. 1996, A&AS, 117, 393
Bertin, E., Mellier, Y., Radovich, M., et al. 2002, in ASP Conf. Ser. 281, Astronomical Data Analysis Software and Systems XI, ed. D. A. Bohlender, D. Durand, & T. H. Handley (San Francisco, CA: ASP), 228
Beuermann, K., Hessman, F. V., Reinsch, K., et al. 1999, A&A, 352, L26
Bloom, J. S., Starr, D. L., Blake, C. H., Skrutskie, M. F., & Falco, E. E. 2006, in ASP Conf. Ser. 351, Astronomical Data Analysis Software and Systems XV, ed. C. Gabriel, C. Arviset, D. Ponz, & S. Enrique (San Francisco, CA: ASP), 751
Breeveld, A. A., Landsman, W., Holland, S. T., et al. 2011, in AIP Conf. Proc. 1358, Gamma Ray Bursts 2010, ed. J. E. McEnery, J. L. Racusin, & N. Gehrels (Melville, NY: AIP), 373 (arXiv:1102.4717)
Burrows, D. N., Hill, J. E., Nousek, J. A., et al. 2005, Space Sci. Rev., 120, 165
Butler, N. R., & Kocevski, D. 2007, ApJ, 663, 407
Butler, N. R., Kocevski, D., Bloom, J. S., & Curtis, J. L. 2007, ApJ, 671, 656
Campana, S., Thöne, C. C., de Ugarte Postigo, A., et al. 2010, MNRAS, 402, 2429
Cenko, S. B., Fox, D. B., Moon, D.-S., et al. 2006, PASP, 118, 1396
Cenko, S. B., Hora, J. L., & Bloom, J. S. 2011, GCN Circ., 11638, 1
Chincarini, G., Mao, J., Margutti, R., et al. 2010, MNRAS, 406, 2113
Covino, S., Ghisellini, G., Lazzati, D., & Malesani, D. 2004, in ASP Conf. Ser. 312, Third Rome Workshop on Gamma-ray Bursts in the Afterglow Era, ed. M. Feroci, F. Frontera, N. Masetti, & L. Piro (San Francisco, CA: ASP), 169
Cucchiara, A., Levan, A. J., Fox, D. B., et al. 2011, ApJ, 736, 7
da Silva, R., Fumagalli, M., Worseck, G., & Prochaska, X. 2011, GCN Circ., 11635, 1
D'Elia, V., Gehrels, N., Gelbord, J. M., et al. 2011, GCN Circ., 11705, 1
Evans, P. A., Beardmore, A. P., Page, K. L., et al. 2007, A&A, 469, 379
Evans, P. A., Beardmore, A. P., Page, K. L., et al. 2009, MNRAS, 397, 1177
Fabricant, D., Cheimets, P., Caldwell, N., & Geary, J. 1998, PASP, 110, 79
Falcone, A. D., Morris, D., Racusin, J., et al. 2007, ApJ, 671, 1921
Fan, Y.-Z., Dai, Z.-G., Huang, Y.-F., & Lu, T. 2002, Chin. J. Astron. Astrophys., 2, 449
Farah, A., Barojas, E., Butler, N. R., et al. 2010, Proc. SPIE, 7735, 77357Z
Filippenko, A. V., Li, W. D., Treffers, R. R., & Modjaz, M. 2001, in ASP Conf. Ser. 246, IAU Colloq. 183: Small Telescope Astronomy on Global Scales, ed. B. Paczynski, W.-P. Chen, & C. Lemme (San Francisco, CA: ASP), 121
Foley, S. 2011, GCN Circ., 11727, 1
Gao, W. 2009, ApJ, 697, 1044
Gao, W.-H. 2011, arXiv:1104.3382
Gehrels, N., Chincarini, G., Giommi, P., et al. 2004, ApJ, 611, 1005
Giannios, D., Mimica, P., Aloy, M. A., et al. 2008, A&A, 478, 747
Golenetskii, S., Aptekar, R., Mazets, E., & Pal'Shin, V. 2011a, GCN Circ., 11659, 1
Golenetskii, S., Aptekar, R., Mazets, E., et al. 2011b, GCN Circ., 11723, 1
Gomboc, A., Kobayashi, S., Guidorzi, C., et al. 2008, ApJ, 687, 443
Gorosabel, J., Duffard, R., Kubanek, P., & Guijarro, A. 2011, GCN Circ., 11696, 1
Granot, J., & Königl, A. 2003, ApJ, 594, L83
Gruber, D., Krühler, T., Foley, S., et al. 2011, A&A, 528, A15
Gruzinov, A., & Waxman, E. 1999, ApJ, 511, 852
Guidorzi, C., Kobayashi, S., Perley, D. A., et al. 2011, arXiv:1105.1591
Guidorzi, C., Monfardini, A., Gomboc, A., et al. 2006, PASP, 118, 288
Hook, I. M., Jørgensen, I., Allington-Smith, J. R., et al. 2004, PASP, 116, 425
Ioka, K., Kobayashi, S., & Zhang, B. 2005, ApJ, 631, 429
Kalberla, P. M. W., Burton, W. B., Hartmann, D., et al. 2005, A&A, 440, 775
Klotz, A., Gendre, B., Stratta, G., et al. 2008, A&A, 483, 847
Kobayashi, S. 2000, ApJ, 545, 807
Kobayashi, S., & Zhang, B. 2003, ApJ, 597, 455
Kobayashi, S., Zhang, B., Mészáros, P., & Burrows, D. 2007, ApJ, 655, 391
Kumar, P., & Panaitescu, A. 2000, ApJ, 541, L51
Kumar, P., & Panaitescu, A. 2003, MNRAS, 346, 905
Lazzati, D., & Begelman, M. C. 2006, ApJ, 641, 972
Lazzati, D., Rossi, E., Covino, S., Ghisellini, G., & Malesani, D. 2002, A&A, 396, L5
Liang, E. W., Zhang, B., O'Brien, P. T., et al. 2006, ApJ, 646, 351
Margutti, R., Bernardini, G., Barniol Duran, R., et al. 2011, MNRAS, 410, 1064
Markwardt, C. B., Barthelmy, S. D., Baumgartner, W. H., et al. 2011, GCN Circ., 11646, 1
Marshall, F. E., Antonelli, L. A., Burrows, D. N., et al. 2011, ApJ, 727, 132
Mészáros, A., Řípa, J., & Ryde, F. 2011, A&A, 529, A55
Mészáros, P. 2006, Rep. Prog. Phys., 69, 2259

Miller, J. S., & Stone, R. 1993, Lick Observatory Technical Report (University of California, Santa Cruz), 48
Molinari, E., Vergani, S. D., Malesani, D., et al. 2007, A&A, 469, L13
Morgan, A. N., & Bloom, J. S. 2011, GCN Circ., 11666, 1
Morgan, A. N., Klein, C. R., & Bloom, J. S. 2011, GCN Circ., 11636, 1
Mundell, C. G., Guidorzi, C., & Steele, I. A. 2010, Advances in Astronomy, 2010, 718468
Mundell, C. G., Melandri, A., Guidorzi, C., et al. 2007a, ApJ, 660, 489
Mundell, C. G., Steele, I. A., Smith, R. J., et al. 2007b, Science, 315, 1822
Oates, S. R., Page, M. J., Schady, P., et al. 2009, MNRAS, 395, 490
Oates, S. R., Page, M. J., Schady, P., et al. 2011, MNRAS, 412, 561
Oke, J. B., & Gunn, J. E. 1983, ApJ, 266, 713
Osborne, J. P., Beardmore, A. P., Evans, P. A., & Goad, M. R. 2011, GCN Circ., 11712, 1
Pal'Shin, V. 2011, GCN Circ., 11697, 1
Panaitescu, A., & Kumar, P. 2002, ApJ, 571, 779
Panaitescu, A., & Vestrand, W. T. 2011, MNRAS, 414, 3357
Perley, D. A., Bloom, J. S., Butler, N. R., et al. 2008, ApJ, 672, 449
Perley, D. A., Bloom, J. S., Klein, C. R., et al. 2010, MNRAS, 406, 2473
Petitpas, G., Zauderer, A., Berger, E., et al. 2011, GCN Circ., 11650, 1
Poole, T. S., Breeveld, A. A., Page, M. J., et al. 2008, MNRAS, 383, 627
Quimby, R. M., Rykoff, E. S., Yost, S. A., et al. 2006, ApJ, 640, 402
Racusin, J. L., Karpov, S. V., Sokolowski, M., et al. 2008, Nature, 455, 183
Racusin, J. L., Liang, E. W., Burrows, D. N., et al. 2009, ApJ, 698, 43
Rees, M. J., & Meszaros, P. 1992, MNRAS, 258, 41P
Roming, P. W. A., Kennedy, T. E., Mason, K. O., et al. 2005, Space Sci. Rev., 120, 95
Rossi, A., Schulze, S., Klose, S., et al. 2011, A&A, 529, A142
Rossi, E. M., Lazzati, D., Salmonson, J. D., & Ghisellini, G. 2004, MNRAS, 354, 86
Rykoff, E. S., Smith, D. A., Price, P. A., et al. 2004, ApJ, 601, 1013
Sakamoto, T., Barthelmy, S. D., Baumgartner, W. H., & Beardmore, A. P. 2011, GCN Circ., 11692, 1
Salvaterra, R., Della Valle, M., Campana, S., et al. 2009, Nature, 461, 1258
Sari, R., & Piran, T. 1997, ApJ, 485, 270
Sari, R., & Piran, T. 1999, ApJ, 520, 641
Sari, R., Piran, T., & Narayan, R. 1998, ApJ, 497, L17
Shao, L., & Dai, Z. G. 2005, ApJ, 633, 1027
Shen, R.-F., & Zhang, B. 2009, MNRAS, 398, 1936
Skrutskie, M. F., Cutri, R. M., Stiening, R., et al. 2006, AJ, 131, 1163
Steele, I. A., Bates, S. D., Guidorzi, C., et al. 2010, Proc. SPIE, 7735, 773549
Stratta, G., & D'Elia, V. 2011, GCN Circ., 11721, 1
Tanvir, N. R., Fox, D. B., Levan, A. J., et al. 2009, Nature, 461, 1254
Totani, T., Kawai, N., Kosugi, G., et al. 2006, PASJ, 58, 485
van der Horst, A. J., Kouveliotou, C., Kamble, A. P., & Wijers, R. A. M. J. 2011, GCN Circ., 11663, 1
Vestrand, W. T., Wren, J. A., Wozniak, P. R., et al. 2006, Nature, 442, 172
Watson, D., Hjorth, J., Fynbo, J. P. U., et al. 2007, ApJ, 660, L101
Zauderer, A., Berger, E., & Frail, D. 2011a, GCN Circ., 11661, 1
Zauderer, A., Frail, D., & Berger, E. 2011b, GCN Circ., 11740, 1
Zhang, B. 2011, C. R. Phys., 12, 206
Zhang, B., Fan, Y. Z., Dyks, J., et al. 2006, ApJ, 642, 354
Zhang, B., Kobayashi, S., & Mészáros, P. 2003, ApJ, 595, 950